Special Topic—Physical research in liquid crystal

Azobenzene mesogens mediated preparation of SnS nanocrystals encapsulated with *in-situ* N-doped carbon and their enhanced electrochemical performance for lithium ion batteries application*

Meng Wang(王勐)[1], Yang Zhou(周旸)[1], Junfei Duan(段军飞)[2,†], and Dongzhong Chen(谌东中)[1,‡]

[1] *Department of Polymer Science and Engineering, Key Laboratory of High Performance Polymer Materials and Technology of Ministry of Education, School of Chemistry and Chemical Engineering, Nanjing University, Nanjing* 210023, *China*

[2] *Department of Physics and Electronic Science, Changsha University of Science and Technology, Changsha* 410076, *China*

(Received 1 June 2016; published online 2 August 2016)

In this work, azobenzene mesogen-containing tin thiolates have been synthesized, which possess ordered lamellar structures persistent to higher temperature and serve as liquid crystalline precursors. Based on the preorganized tin thiolate precursors, SnS nanocrystals encapsulated with *in-situ* N-doped carbon layer have been achieved through a simple solventless pyrolysis process with the azobenzene mesogenic thiolate precursor served as Sn, S, N, and C sources simultaneously. Thus prepared nanocomposite materials as anode of lithium ion batteries present a large specific capacity of 604.6 mAh·g^{-1} at a current density of 100 mA·g^{-1}, keeping a high capacity retention up to 96% after 80 cycles, and display high rate capability due to the synergistic effect of well-dispersed SnS nanocrystals and N-doped carbon layer. Such encouraging results shed a light on the controlled preparation of advanced nanocomposites based on liquid crystalline metallomesogen precursors and may boost their novel intriguing applications.

Keywords: azobenzene-containing tin thiolates, liquid crystalline precursor, controlled synthesis, *in-situ* N-doped

PACS: 61.30.–v, 81.07.Bc, 82.47.Aa **DOI:** 10.1088/1674-1056/25/9/096102

1. Introduction

Metallomesogens have attracted tremendous interest in recent decades owing to their combining some features of metal ions and liquid crystals (LCs) with abundant characteristics such as thermochromic, optical, electronic, and magnetic properties compared with organic liquid crystals.[1–10] Wang and co-workers reported phosphorescent metallomesogens with various LC phases of smectic, columnar, and micellar cubic for high efficiency organic light-emitting diode (OLED) application.[11] Ag nanowires were prepared through thermolysis of polynuclear silver (I) triazole metallomesogens in their assembled SmA mesophase, providing a simple method to prepare silver conducting films for electronic devices.[12] Upon introducing mesogenic units such as azobenzene, LC-mediated nanoparticles (NPs), their self-assembly arrays can be achieved to construct well-defined functional nanomaterials.[13,14] In our previous work, a systematic investigation on the azobenzene-containing metallomesogens and their metal thiolate precursors mediated controlled preparation and *in-situ* assembly of multiple morphological metal and metal sulfide nanomaterials such as Au nanoparticles,[15] Ag nanodisks,[16] and Cu_2S nanowires has been carried out through solventless pyrolysis.

On the other hand, rapid development of portable electronics and electric vehicles stimulates the research of energy-efficient and environment-friendly energy storage devices. Since nanostructured electrode materials offer controllable surface area, short diffusion path, and effective buffer for volume change, various nanostructured materials for energy storage and conversion, such as 3D graphene hierarchical porous carbon/metal (metal oxide) composite based on metal organic frameworks (MOFs) as templates or precursors, have aroused increasing attention in recent years.[17–20] Our azobenzene-containing metallomesogens possessed persistent ordered mesostructures bearing some common characteristics with MOFs, which inspired us to further explore their potential applications in advanced energy materials. Tin mono-sulfide (SnS) has shown great advantages as potential alterative anode materials for lithium ion batteries (LIBs) thanks to its high theoretical capacity (782 mAh·g^{-1}), security and low cost.[21–23] However, its application in LIBs was severely restricted by the huge volume expansion thus an associated rapid capacity fading during the lithiation/delithiation process. Up to now, mainly two effective ways to significantly overcome such insufficiency have been adopted. One method was to build SnS nanomaterials with special structures and morphologies such as nanoparticles, nanorods, nanoribbons, and nanoflowers, for

*Project supported by the National Natural Science Foundation of China (Grant No. 21574062) and the Huaian High-Technology Research Institute of Nanjing University, China (Grant No. 2011Q1).

†Corresponding author. E-mail: junfei_duan@yahoo.com

‡Corresponding author. E-mail: cdz@nju.edu.cn

© 2016 Chinese Physical Society and IOP Publishing Ltd

shortening the Li^+ transport path length and providing high rate capacity.[23–27] Nevertheless, the aggregation of nanocrystals during the charge/discharge process is still unsolved. The other method included a proper combination of SnS with carbon materials to improve the conductivity and alleviate the volume expansion during cycling.[28,29] Whereas the traditional carbon coating method is not an effective technique to realize uniform carbon coating on the surface of electrode materials, which can significantly affect the cycling performance of anodes. Meanwhile, nitrogen doping in coated carbon has often been conducted for its high electric conductivity and more active sites for Li^+ intercalation/deintercalation,[30,31] and few studies have been reported on SnS nanoparticles with evenly coated N-doped carbon.

Herein, azobenzene-containing tin thiolates showing smectic (Sm) LC mesophase have been synthesized, then SnS nanocomposites encapsulated with *in situ* N-doped carbon layer further prepared via a simple solventless pyrolysis process of the tin thiolate precursors serving as Sn, S, N, and C sources simultaneously. Furthermore, the carbon layers were evenly coated on the surface of SnS nanoparticles. To our knowledge, this is the first time that *in situ* N-doped carbon evenly coated SnS nanoparticles has been obtained through a simple solventless pyrolysis process of a single precursor, and the as-prepared nanocomposites exhibited good cycling performance. High rate capacity as LIBs anodes, owing to the synergistic effect of well-prepared SnS nanocrystals and coated N-doped carbon layer.

2. Experimental section

2.1. Materials

The preparation of azobenzene mesogenic thiol ligand with six methylene spacer and decyloxy tail $C_{10}H_{21}O$-Ph-N=N-Ph-$C_6H_{12}SH$ was conducted according to our previously reported procedures.[16] The raw material Sn (II) chloride dihydrate (98%) was provided by Alfa Aesar and used without purification. All of the other chemical reagents were purified with standard procedures.

2.2. Synthesis

The synthesis procedure of the azobenzene mesogenic tin thiolate is illustrated in Fig. 1. In a typical synthesis, 4-(6-mercaptohexyloxy)-4′-decyloxy-azobenzene (1.50 g, 3.19 mmol) and Sn (II) chloride dihydrate (360 mg, 1.59 mmol) were, respectively, dissolved in tetrahydrofuran (THF) by ultrasonication. Then, the Sn (II) chloride solution was added into the 4-(6-mercaptohexyloxy)-4′-decyloxy-azobenzene solution dropwise with slow magnetic stirring for 30 min at room temperature. The precipitate formed was collected after several washing-centrifugation cycles and dried at 45 °C under vacuum overnight to obtain azobenzene-containing tin thiolate as the precursor compound, and then the precursor was carbonized at 600 °C for 2 h under Ar atmosphere with a heating rate of 2 °C·min^{-1} to achieve SnS@N/C composite.

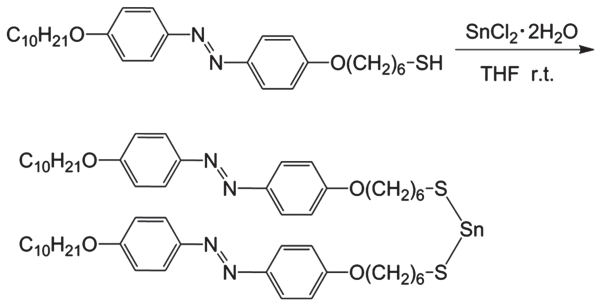


Fig. 1. Preparation of the precursor azobenzene-containing tin thiolate.

2.3. Characterization

The x-ray diffraction (Bruker D8 Advance diffractometer) and transmission electron microscopy (TEM, JEOL, JEM-2100) were employed for the structure and morphology investigation. Differential scanning calorimetry (DSC) analyses were carried out on a Mettler Toledo calorimeter associated with a cooling accessory with a 10 °C·min^{-1} heating or cooling rate under N_2 gas flow. Small-angle x-ray scattering (SAXS) investigation was performed on a high-flux instrument (SAXSess mc^2, Anton Paar) with an imaging-plate (IP) spanning broad q ranging from 0.06 nm^{-1} to 29 nm^{-1}, with $q = (4\pi \sin\theta)/\lambda$, Cu K_α radiation $\lambda = 0.1542$ nm, collecting at 40 kV/50 mA for 5 min. Typically, aluminum foil was used for the powder sample encapsulation and the collected x-ray analysis data were processed with the associated SAXSquant software 3.80. Polarized optical microscopy (POM) observation and photography were conducted on a PM6000 optical microscope associated with a Leitz-350 heating stage and a Nikon (D3100) digital camera. Raman spectra were recorded using a Renishaw 1000 spectrometer system with a 633-nm He–Ne laser operating at 2 mW with 10 s exposure time. The x-ray photoelectron spectroscopy (XPS) analysis was performed on a PHI 5000 Versa probe system, using monochromatic Al K_α radiation (1486.6 eV) operating at 25 W.

2.4. Electrochemical analysis

Electrochemical measurements were performed using 2032 type coin cells. The working electrode slurry consisted of active material (70 wt%), conducting carbon (20 wt%), and polyvinyldifluoride (PVDF, 10 wt%) in N-methylpyrrolidone (NMP) and was coated onto a copper foil current collector. The above slurry was dried at 110 °C in a vacuum oven and Li foil was taken as the counter electrode. Coin cells were assembled in an argon-filled glove-box with an electrolyte of 1M $LiPF_6$ in an ethylene carbonate and diethyl carbonate (EC/DMC, 1:1 volume) mixture, and Celgard 2500 separator was used. Electrochemical tests were conducted using an automatic galvanostatic charge–discharge unit, Land CT2001 sys-

tem, with a potential range of 0–2.0 V versus Li/Li$^+$ electrode at room temperature.

3. Results and discussion

3.1. Structural and morphological characterizations

The thermal properties of precursor compound azobenzene-containing tin thiolate and its corresponding ligand mesogenic thiol were investigated by DSC for comparison, and the thermograms of the first cooling and second heating cycles are shown in Fig. 2(a). The azobenzene thiol exhibits a 30 K interval smectic (SmA) LC mesophase, as revealed by the typical focal conic POM texture (Fig. 3(b)). The azobenzene-containing tin thiolate shows a lamellar mesophase with focal conic mosaic POM texture (Fig. 3(d)) similar to the smectic phase of mesogenic thiol.

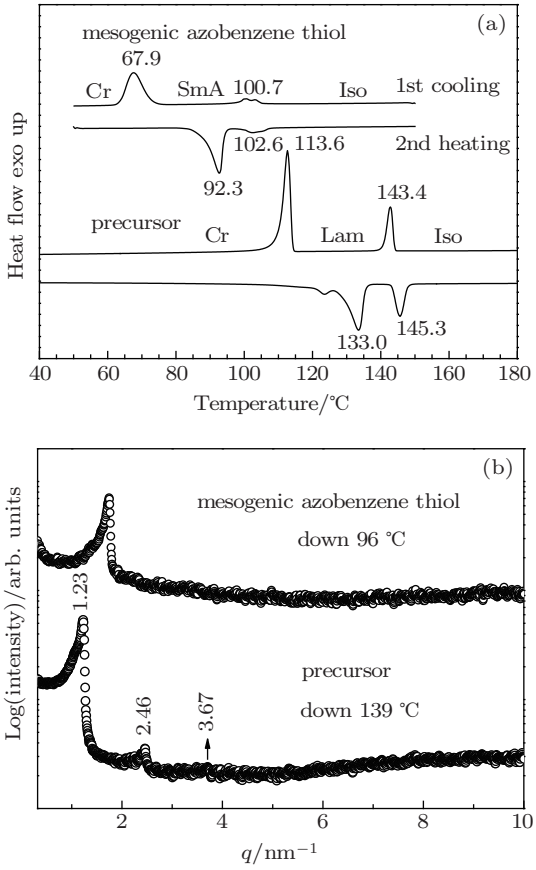


Fig. 2. (a) DSC thermograms of mesogenic azobenzene thiol and tin thiolate precursor during the 1st cooling and 2nd heating scans at a rate of 10 °C·min^{-1}. (b) SAXS profiles of ligand thiol and the precursor tin thiolate at their LC state.

Moreover, SAXS investigation was performed to probe into the ordered structure and phase behavior of the tin thiolate precursor and the corresponding mesogenic azobeneze thoil. Figure 2(b) shows the SAXS profiles of the ligand and precursor samples at their LC state. The precursor demonstrated a more organized lamellar structure compared with its mesogenic azobenzene thiol. For the tin thiolate precursor, upon cooling down to the mesophase state at 139 °C, in between the temperature range 145 °C and 133 °C consistent with the DSC measurement, three reflections existed in the small-angle range with q values of 1.23 nm^{-1}, 2.46 nm^{-1}, 3.67 nm^{-1} in ratio of 1:2:3, indicating an ordered lamellar mesophase. Therefore, it is worth noting that the precursor metal thiolates well inherited the liquid crystallinity of the corresponding ligand mesogenic thiols with enhanced heat resistance in virtue of the introduction of metal ions such as tin in this case.[15,16]

Figure 4(a) presents the XRD patterns of as-prepared SnS@N/C nanocomposite. All the diffraction peaks can be easily attributed to orthorhombic SnS crystal (JSPDS card No. 39-0354). No diffraction signals from precursor or other impurities were observed, suggesting complete conversion of the precursor into SnS nanocrystals with sharp peaks compared to the standard line-style diffractions of SnS single crystal. Raman spectrum of the composites as shown in Fig. 4(b) with two broad peaks at 1341 cm^{-1} and 1583 cm^{-1} respectively at an intensity ratio of 0.95 could be well assigned to typical D and G bands of amorphous carbon, manifested the amorphous character of the coated carbon layer.[32] Generally, the conductive amorphous carbon matrix with porous structure not only favors the diffusion of lithium ions, but also provides a buffer layer to cushion the large volume change during the lithiation–delithiation, contributing to the significantly improved cycling performance and overall capacity.[33]

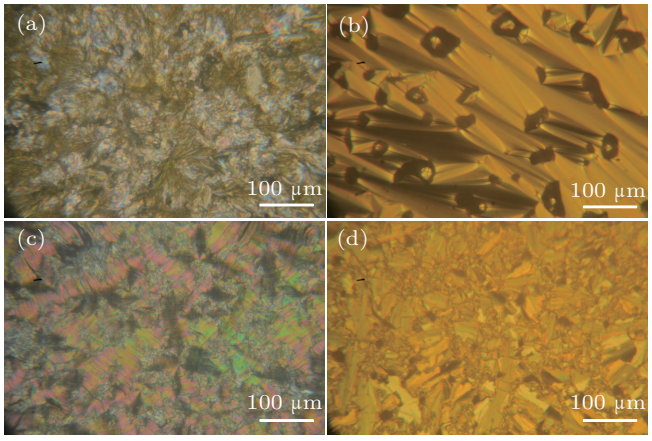


Fig. 3. (color online) Representative POM images of mesogenic azobenzene thiol at (a) 55 °C, Cr; (b) 92 °C, SmA; and precursor tin thiolate at (c) 90 °C, Cr; (d) 134 °C, lamellar phase.

The surface composition of the SnS@N/C nanocomposite was investigated by x-ray photoelectron spectroscopy (XPS). Figure 4(c) shows the full XPS spectrum of the SnS@N/C nanocomposite with signals of all concerned elements Sn, S, C, N, and O, demonstrating that the formation of SnS nanocrystals coated with N-doped carbon SnS@N/C, with the content of N species in the nanocomposite was determined to be 7.04 wt% based on the elemental analysis. It should be mentioned that many researchers have revealed that nitrogen doping is an efficient way to boost the electrochemical performance of the carbon based materials, thanks not only to their

enhancing the electric conductivity, but also offering more active sites for lithium ion insertion and extraction, thus benefiting for the improved cycling performance and rate capacity of the electrode.[31] As shown in Fig. 4(d), the high resolution Sn 3d spectrum displays two characteristic peaks at 486.4 eV (Sn $3d_{5/2}$) and 494.7 eV (Sn $3d_{3/2}$), manifesting that some SnS nanoparticles close to the surface of the carbon material were oxidized into SnO_2, which explained the existence of element O in the full XPS spectra. Nevertheless, the occurrence of little SnO_2 might increase the general capacity of the material in view of the much higher theoretical capacity of SnO_2 (1494 mAh·g^{-1}) compared to that of SnS (782 mAh·g^{-1}).[34]

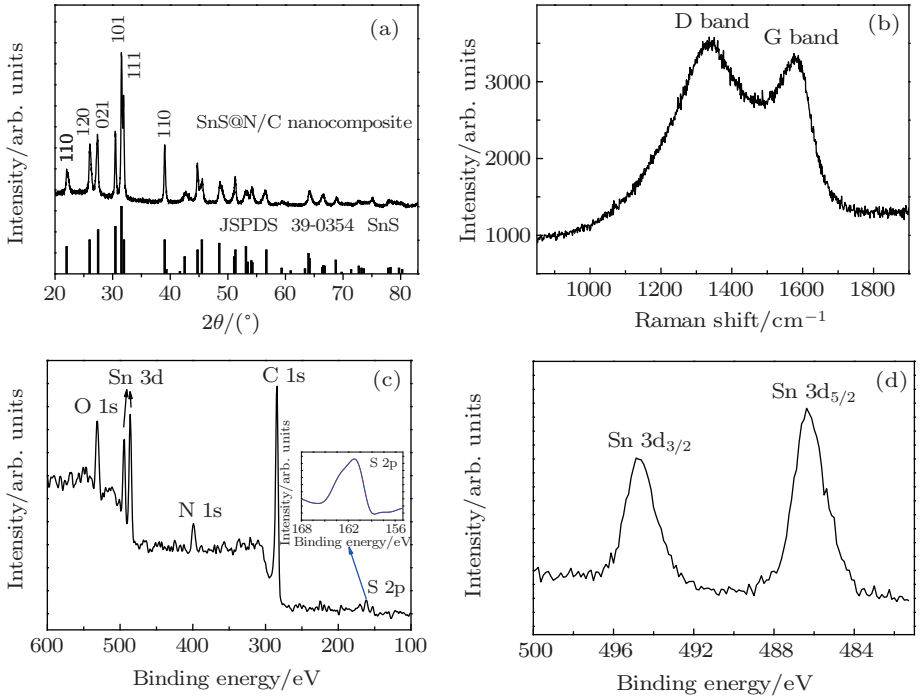


Fig. 4. (color online) (a) XRD patterns of SnS@N/C nanocomposite and pure SnS crystal (JCPDS card No. 39-0354). (b) Raman spectra of the SnS@N/C nanocomposite. (c) The full XPS spectrum of as-prepared SnS@N/C nanocomposite with the inset showing the S 2p spectrum in magnified scale. (d) High-resolution XPS spectra of Sn 3d.

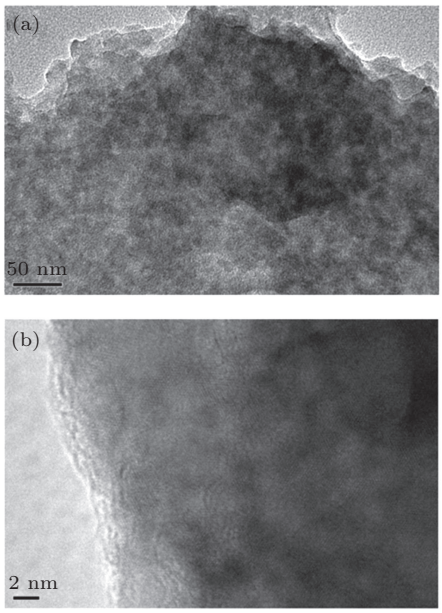


Fig. 5. (a) Transmission electron microscopy (TEM). (b) High-resolution TEM (HRTEM) images of SnS@N/C nanocomposite.

Transmission electron microscopy (TEM) was used to investigate the morphology of the as-prepared SnS@N/C nanocomposite. As shown in Fig. 5(a), SnS nanoparticles (dark dots) with relatively uniform size were found to be homogenously inserted onto the carbon layer, possessing an average size of around 4 nm as measured from the high-revolution TEM (HRTEM) image shown in Fig. 5(b).

3.2. Electrochemical performance of SnS@N/C nanocomposite

The electrochemical behavior of the nanocomposites was investigated through evaluation with the nanocomposite based materials as anodes of LIBs. The rate performance of the SnS@N/C composite anode was assessed with the cell cycled at various current densities from 100 mA·g^{-1} to 1000 mA·g^{-1}. As shown in Fig. 6(a), the nanocomposite offered a reversible capacity of about 604.6 mAh·g^{-1}, 532.6 mAh·g^{-1}, 389.0 mAh·g^{-1}, and 300.4 mAh·g^{-1} at the current density of 100 mA·g^{-1}, 200 mA·g^{-1}, 500 mA·g^{-1}, and 1000 mA·g^{-1}, respectively. The capacity could recover to 587.7 mAh·g^{-1} when the current density returned to 100 mA·g^{-1}, which is close to the original level, suggesting that the morphology of the as-prepared SnS@N/C composite was well preserved during cycling. The good rate capacity of the SnS@N/C

nanocomposite originated from the combination of nano-sized SnS particles, uniform distribution and N-doped carbon coating layer. Figure 6(b) shows the cycling performance of the SnS@N/C nanocomposite anode at a scan rate of 100 mA·g^{-1}. Upon cycling, the discharge and charge capability slightly decreased at the beginning for several cycles and then leveled off with a high columbic efficiency of up to 99%. After 90 cycles, the discharge and charge capacity still maintained 493.4 mAh·g^{-1} and 477.9 mAh·g^{-1}, respectively. These results revealed that the SnS@N/C nanocomposite demonstrated quite good cycle stability.

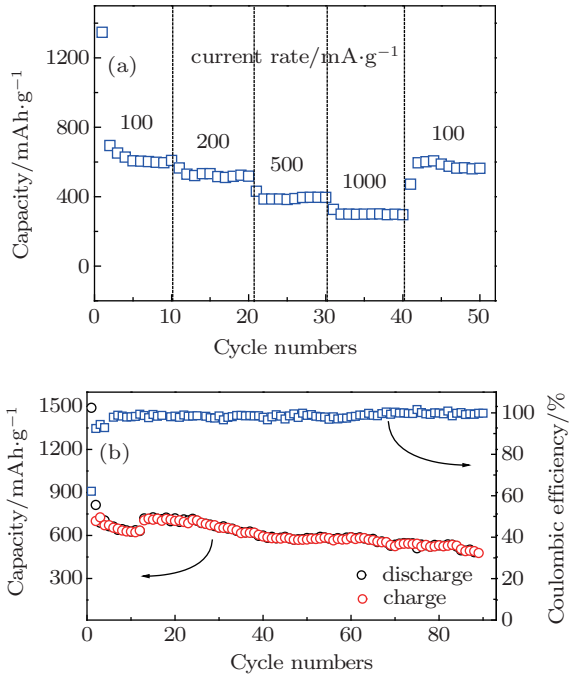


Fig. 6. (color online) (a) Rate performance of SnS@N/C nanocomposite anode at various current rates. (b) Cycling performance of SnS@N/C nanocomposite anode at a rate of 100 mA·g^{-1}.

4. Conclusion

In summary, with the introduction of azobenzene mesogen into the tin thiolate, an ordered lamellar structure persistent to higher temperature has been achieved. Then nitrogen-doped carbon encapsulated SnS nanocomposites have been obtained through solventless thermolysis of the metallomesogenic precursor which served as carbon, nitrogen and tin sources simultaneously in a preorganized state up to higher temperature. The electrochemical performance of the SnS@N/C nanocomposite was evaluated as an anode material of LIBs, which provided a capacity of 604.6 mAh·g^{-1} at a current density of 100 mA·g^{-1} and the capacity retention up to 96% after 80 cycles. The excellent battery performance originated from the uniform size of SnS nanoparticles and N-doped carbon layer. The *in-situ* N-doped carbon coating of SnS nanocrystals can significantly enhance the electron conductivity, prevent the aggregation of SnS nanoparticles and effectively protect from the volume expansion during lithiation/delithiation process. Such encouraging results shed light on the controlled preparation of liquid crystalline precursor mediated nanostructured materials, which may boost extensive fascinating applications of advanced nanocomposites.

References

[1] Donnio B 2014 *Inorg. Chim. Acta* **409** 53
[2] Binnemans K 2009 *J. Mater. Chem.* **19** 448
[3] Date R W, Iglesias E F, Rowe K E, Elliott J M and Bruce D W 2003 *Dalton Trans.* **10** 1914
[4] Xiao X S, Lu W and Che C M 2014 *Chem. Sci.* **5** 2482
[5] Kaur R and Mehta S K 2014 *Coord. Chem. Rev.* **262** 37
[6] Ma H, Jiang L L, Li M, Li C X and Jiang Y R 2013 *Chin. J. Liquid Cryst. Displ.* **28** 653
[7] Pang H, Zheng C W, Cao J H, Zhang X and Hua R M 2015 *Chin. J. Liquid Cryst. Displ.* **30** 752
[8] Matioli E, Brinkley S, Kelchner K M, Hu Y L, Nakamura S, DenBaars S, Speck J and Weisbuch C 2012 *Light Sci. Appl.* **1** e22
[9] Wang L, Lin X W, Hu W, Shao G H, Chen P, Liang L J, Jin B B, Wu P H, Qian H, Lu Y N, Liang X, Zheng Z G and Lu Y Q 2015 *Light Sci. Appl.* **4** e253
[10] He Z H, Chen C P, Zhu J L, Yuan Y C, Li Y, Hu W, Li X, Li H J, Lu J G and Su Y K 2015 *Chin. Phys. B* **24** 064203
[11] Wang Y, Shi J, Chen J, Zhu W and Baranoff E 2015 *J. Mater. Chem. C* **3** 7993
[12] Su P Y S, Hsu S J, Tseng J C W, Hsu H F, Wang W J and Lin I J B 2016 *Chem. Eur. J.* **22** 323
[13] Bisoyi H K and Kumar S 2011 *Chem. Soc. Rev.* **40** 306
[14] Nealon G L, Greget R, Dominguez C, Nagy Z T, Guillon D, Gallani J L and Donnio B 2012 *Beilstein J. Org. Chem.* **8** 349
[15] Duan J, Wang M, Bian H, Zhou Y, Ma J, Liu C and Chen D 2014 *Mater. Chem. Phys.* **148** 1013
[16] Duan J, Ma J, Wu B, Li Q, Fang J and Chen D 2014 *J. Mater. Chem. C* **2** 2375
[17] Cao X, Zheng B, Rui X, Shi W, Yan Q and Zhang H 2014 *Angew. Chem.* **126** 1428
[18] Cao X, Yin Z and Zhang H 2014 *Energy Environ. Sci.* **7** 1850
[19] Kim T K, Lee K J, Cheon J Y, Lee J H, Joo S H and Moon H R 2013 *J. Am. Chem. Soc.* **135** 8940
[20] Yang S J, Nam S, Kim T, Im J H, Jung H, Kang J H, Wi S, Park B and Park C R 2013 *J. Am. Chem. Soc.* **135** 7394
[21] Li Y, Tu J P, Huang X H, Wu H M and Yuan Y F 2007 *Electrochem. Commun.* **9** 49
[22] Tao H C, Yang X L, Zhang L L and Ni S B 2014 *J. Electroanal. Chem.* **728** 134
[23] Tripathi A M and Mitra S 2014 *Rsc Adv.* **4** 10358
[24] Li S, Zheng J, Hu Z, Zuo S, Wu Z, Yan P and Pan F 2015 *RSC Adv.* **5** 72857
[25] Hongtao L, Yan L, Zan W and Ping H 2010 *Nanotechnology* **21** 105707
[26] Deng Z, Cao D, He J, Lin S, Lindsay S M and Liu Y 2012 *ACS Nano* **6** 6197
[27] Biacchi A J, Vaughn D D and Schaak R E 2013 *J. Am. Chem. Soc.* **135** 11634
[28] Zhu J, Wang D and Liu T 2013 *Appl. Sur. Sci.* **282** 947
[29] Li S, Zuo S, Wu Z, Liu Y, Zhuo R, Feng J, Yan D, Wang J and Yan P 2014 *Electrochim. Acta* **136** 355
[30] Peng H J, Hou T Z, Zhang Q, Huang J Q, Cheng X B, Guo M Q, Yuan Z, He L Y and Wei F 2014 *Adv. Mater. Interfaces* **1** 1400227
[31] Qie L, Chen W M, Wang Z H, Shao Q G, Li X, Yuan L X, Hu X L, Zhang W X and Huang Y H 2012 *Adv. Mater.* **24** 2047
[32] Kim C, Yang K S, Kojima M, Yoshida K, Kim Y J, Kim Y A and Endo M 2006 *Adv. Func. Mater.* **16** 2393
[33] Zhu Z, Cheng F and Chen J 2013 *J. Mater. Chem. A* **1** 9484
[34] Zhou X, Wan L J and Guo Y G 2013 *Adv. Mater.* **25** 2152